Scanning total internal reflection fluorescence microscopy under one-photon and two-photon excitation: image formation

James W. M. Chon and Min Gu

We propose a new type of total internal reflection fluorescence microscopy (TIRFM) called scanning TIRFM (STIRFM) that uses a focused ring-beam illumination and a high-numerical-aperture objective (NA = 1.65). The evanescent field produced by the STIRFM is focused laterally, producing a small excitation volume that can induce a nonlinear effect such as two-photon absorption. Experimental images of CdSe quantum dot nanocrystals and Rhodamine 6G–doped microbeads show that good lateral and axial resolutions are achieved with the current setup. The theoretical simulation of the focal spot produced in STIRFM geometry shows that the focused evanescent field is split into two peaks because of the depolarization effect of a high numerical-aperture objective lens. However, the point-spread function analysis of both one-photon and two-photon excitation cases shows that the detection of the focus-splitting effect is dependent on the detection pinhole size. The effect of pinhole size on image formation is theoretically investigated and confirmed experimentally with the nanocrystal images.

OCIS codes: 110.0180, 180.2520, 180.5810, 190.4180.

1. Introduction

In the field of fluorescence microscopy, total internal reflection fluorescence microscopy (TIRFM) and spectroscopy have been major techniques in many applications, such as fluorescence kinetic studies of fluorophores at solid–liquid interfaces,[1,2] fluorescence lifetime imaging of living cells,[3,4] and single molecular detections.[5–12] The ability to strongly reduce background fluorescence from aqueous solutions has been their major contribution. Such suppression of background fluorescence is achieved by a totally internally reflected laser beam at the interface between the cover glass surface and the aqueous solution, producing a nonpropagating evanescent field just beyond the interface, with a penetration depth of less than 100 nm. In this way only the fluorescent molecules near the interface are excited, creating an extremely thin optical section that leads to images of high contrast.

At present, there are two types of TIRFM, the prism type[1–6,8–12] and the objective type.[5–7] In a prism-type TIRFM, an evanescent field is generated at the interface between the prism and a sample by direction of a laser beam at an angle larger than the critical angle, and the fluorescence is collected by an objective. In an objective-type TIRFM, a high-numerical-aperture (NA) objective of ~1.3–1.4 is used to both excite an evanescent field and to collect the fluorescence, thereby eliminating the placement of a prism. The inherent disadvantage of the objective-type TIRFM is that only a small portion of the objective is utilized in generating an evanescent field; consequently, positioning and focusing the laser beam onto the objective is difficult and tedious.

In this paper we propose a new type of TIRFM called scanning TIRFM (henceforth abbreviated STIRFM), using a high-NA objective of 1.65 illuminated by a ring beam. In STIRFM the generation of an evanescent field is achieved by focusing the ring-beam illumination at the interface. The ring-beam illumination is produced by blocking a central portion of a circular beam with an obstruction disk, whose maximum convergence angle is equal to or larger than the critical angle (see Fig. 1). Subsequently, all

The authors are with the Centre for Micro-Photonics, School of Biophysical Sciences and Electrical Engineering, Swinburn University of Technology, P.O. Box 218, Hawthorn, 3122, Australia. J. Chon's e-mail address is jchon@swin.edu.au.

Received 10 April 2003; revised manuscript received 27 October 2003; accepted 28 October 2003.

0003-6935/04/051063-09$15.00/0

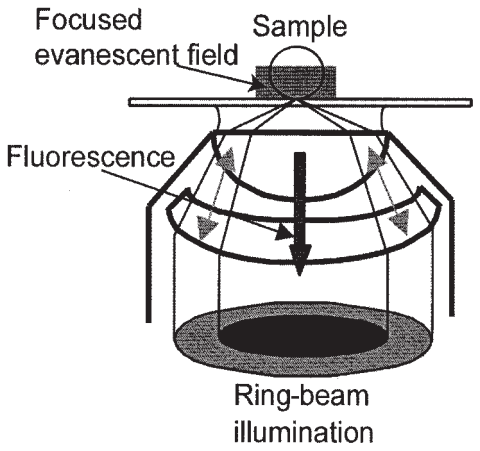

Fig. 1. Concept of STIRFM. The focused evanescent field is produced by focusing the ring-beam illumination at the interface between a coverslip glass and a sample medium by a high-NA (1.65) objective. The ring beam is produced by centrally obstructing the beam with a circular disk.

of the ring-beam illumination is totally internally reflected to produce an evanescent field at the interface. Although ring-beam illumination with a high-NA objective lens has been previously used in studying the orientation of single molecules,[13–15] the obstruction disk used in these studies opens the propagating components, and therefore the geometry is not that of a TIRFM in a strict sense.

The geometry of STIRFM has several advantages over other types of TIRFM. First, with a high-NA objective, the portion of the objective that can be utilized to produce an evanescent field is significantly increased. Second, penetration depth control of the evanescent field is made possible by adjustment of the obstruction disk diameter. Third, because the ring beam is focused at the interface, the resulting evanescent field is localized in a very small volume. This small volume can induce fluorescence in a small area without exciting the neighboring molecules, which consequently enhances the signal-to-background ratio and increases the resolution. Furthermore, with a highly focused beam, it would also be possible to induce a nonlinear effect such as two-photon absorption at the focus.

The aim of this paper is to characterize the single- and two-photon imaging performance of STIRFM and to compare it with the point-spread function (PSF) analysis. In Section 2 we present the theoretical simulation of the evanescent focal shape produced by the geometry of STIRFM, and in Section 3 we discuss the single- and two-photon image formation in STIRFM. In Section 4 the experimental setup and the experimental results of STIRFM are presented to verify the imaging capabilities of the current setup. In particular, we present the images of CdSe quantum dots and Rhodamine 6G–doped microbeads to characterize the imaging resolution, the focal shape, and the evanescent field depth of STIRFM. Finally, we present our conclusions in Section 5.

2. Theoretical Simulation of Focus Produced by STIRFM

In STIRFM, shown in Fig. 1, focusing with a high-NA objective induces the depolarization of the input beam. To account for the depolarization effect in simulations of the focus produced by STIRFM, the vectorial Debye theory is employed.[16,17] When a linearly polarized coherent monochromatic plane light wave is focused through an index-mismatched interface by a high-NA objective, the electric field in the focal region of the objective[16,17] can be expressed as

$$\mathbf{E}(r_2, \phi, z_2) = \frac{\pi i}{\lambda}\{[I_0 + \cos(2\phi)I_2]\mathbf{i} + \sin(2\phi)I_2\mathbf{j} + 2i\cos\phi I_1\mathbf{k}\}, \quad (1)$$

where $\mathbf{i}$, $\mathbf{j}$, and $\mathbf{k}$ are the unit vectors in the x, y, and z directions, respectively. The incident polarization is assumed in the x direction. It is clear that $\mathbf{E}$ is depolarized and has three components E_x, E_y, and E_z. Variables r_2, ϕ, and z_2 are the cylindrical coordinates of an observation point. Here the definition of three variables I_0, I_1, and I_2 is given by

$$I_0 = \int_\beta^\alpha (\cos\theta_1)^{1/2}\sin\theta_1(t_s + t_p\cos\theta_2)\exp[-ik_0\Phi(\theta_1)]J_0(k_1r_2\sin\theta_1)\exp(-ik_2z_2\cos\theta_2)\mathrm{d}\theta_1, \quad (2)$$

$$I_1 = \int_\beta^\alpha (\cos\theta_1)^{1/2}\sin\theta_1(t_p\sin\theta_2)\exp[-ik_0\Phi(\theta_1)]J_1(k_1r_2\sin\theta_1)\exp(-ik_2z_2\cos\theta_2)\mathrm{d}\theta_1, \quad (3)$$

$$I_2 = \int_\beta^\alpha (\cos\theta_1)^{1/2}\sin\theta_1(t_s - t_p\cos\theta_2)\exp[-ik_0\Phi(\theta_1)]J_2(k_1r_2\sin\theta_1)\exp(-ik_2z_2\cos\theta_2)\mathrm{d}\theta_1, \quad (4)$$

where $J_0(x)$, $J_1(x)$, and $J_2(x)$ are the zero-, first-, and second-order Bessel functions of the first kind, respectively; α and β are the convergence angles of the waves corresponding to the outer and inner radii of a ring beam, respectively; and t_s and t_p are the Fresnel amplitude transmission coefficients for different polarization states. The aberration cor-

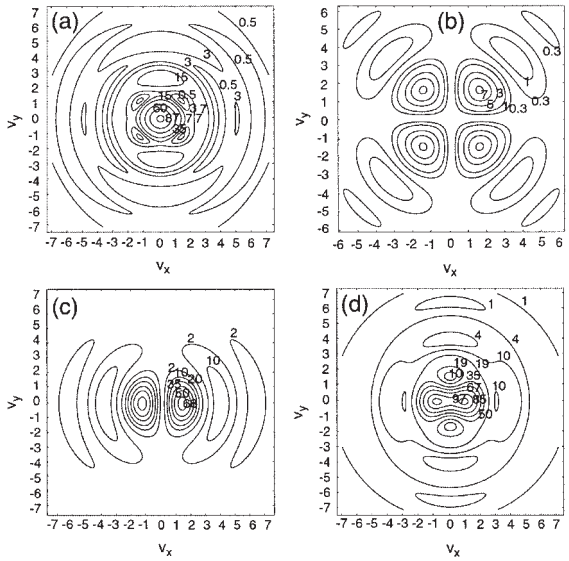

Fig. 2. Contour plots of intensity near the evanescent focus of an objective (NA = 1.65) illuminated by a ring beam (ε = 0.6): (a) $|E_x|^2$, (b) $|E_y|^2$, (c) $|E_z|^2$, (d) $|\mathbf{E}|^2$. Peak intensities of $|\mathbf{E}|^2$ have been normalized to 100, and the incident polarization is parallel to the x axis. The NA is assumed to be 1.65.

rection function $\Phi(\theta_1)$ is given by

$$\Phi(\theta_1) = -d(n_1 \cos\theta_1 - n_2 \cos\theta_2), \qquad (5)$$

where d is the distance between the interface and the focal point of the objective. The intensity is proportional to the modulus squared of Eq. (1).

Figure 2 gives the contour plots ($v_x = kx \sin\alpha$ and $v_y = ky \sin\alpha$) of the normalized intensity $|\mathbf{E}|^2$ and its components $|E_x|^2$, $|E_y|^2$, and $|E_z|^2$ in the x, y, and z directions near the focal region at the coverslip glass ($n = 1.78$) and air interface ($d = 0$), when an objective of NA = 1.65 is illuminated by a ring beam [ε, obstruction radius normalized by the radius of the objective aperture; ε_c, obstruction radius corresponding to the critical angle; $\varepsilon_{\text{outer}} = 1$ (i.e., $\alpha = 68°$) and $\varepsilon_{\text{inner}} = \varepsilon_c$ (i.e., $\beta = 35°$)]. Because the inner radius of the ring beam is calculated to be equal to the critical radius (ε_c), the produced focus is evanescent in nature. As expected, because of the factors $\cos(2\phi)$, $\sin(2\phi)$, and $\cos(\phi)$ in Eq. (1) and because of the relative strength of the Bessel functions, $J_0(x)$, $J_1(x)$, and $J_2(x)$, the patterns of $|E_x|^2$, $|E_y|^2$, and $|E_z|^2$ exhibit one, four, and two lobes, respectively. The splitting of the focus in the direction of polarization (x direction) is visibly clear in the $|\mathbf{E}|^2$ distribution [see Fig. 2(d)], and it is induced by the contribution from $|E_z|^2$. Similar to the free-space splitting, the relative strength or the weighting of the $|E_z|^2$ to the $|E_x|^2$ component governs the overall shape of the focus.[18]

To quantify the relative strength of the $|E_z|^2$ and $|E_x|^2$ components with respect to the inner radius ε of a ring beam, the peak intensity ratio of $|E_z|^2/|E_x|^2$ as a function of the obstruction radius ε is presented in Fig. 3(a), where the NA = 1.65. Three cases of the index-mismatch geometry are assumed: immersion oil ($n = 1.78$) to glass ($n = 1.52$), oil to water ($n = 1.33$), and oil to air. It is seen that $|E_z|^2/|E_x|^2$ ratios increase as the obstruction radius becomes large, peak at the critical radius ε_c, and then start to decrease. This indicates that the depolarization in the

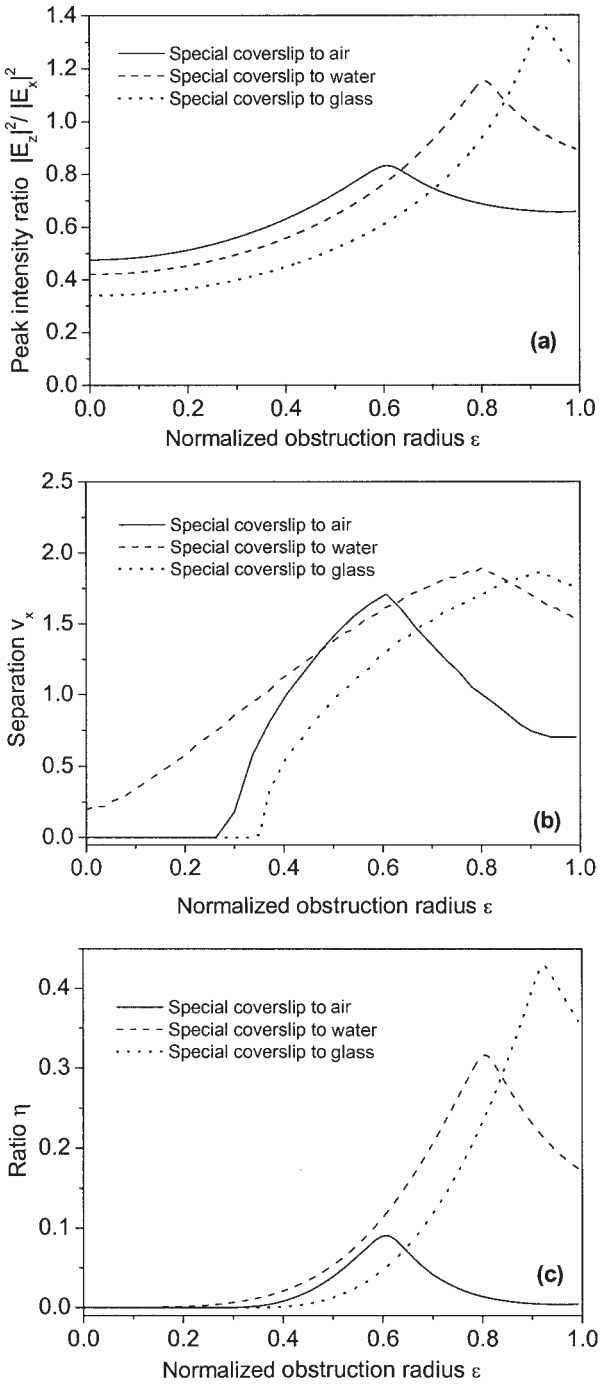

Fig. 3. Plots of (a) the peak intensity ratio of $|E_z|^2/|E_x|^2$, (b) the peak separation Δv_x, and (c) the normalized dip depth η with respect to the normalized obstruction radius ε. The NA of the objective is 1.65. Plots (a), (b), and (c) correspond to the interfaces between immersion oil ($n = 1.78$) and air, between immersion oil and water, and between immersion oil and glass ($n = 1.52$), respectively.

z direction is greatest when the convergence angle is near the critical angle. The decrease in the $|E_z|^2/|E_x|^2$ ratio after the critical angle is due to the fact that, for p-polarization case, the $|E_z|^2$ component of an evanescent field decreases faster than the $|E_x|^2$ component as the incident angle further increases from the critical angle.[6] For an s-polarized evanescent field, the $|E_z|^2$ component is obviously absent. Therefore, in our geometry the integration over the azimuthal angle includes both cases of p- and s-polarization, resulting in a stronger $|E_x|^2$ component.

The characteristic shape of the two-peak focus can be described by the peak-to-peak separation distance expressed by the optical coordinate $\Delta\nu$ and the normalized dip depth η (defined as the ratio of the dip depth between the two peaks to the peak intensity). The separation $\Delta\nu$ and the normalized dip depth η versus the normalized obstruction radius ε are presented in Figs. 3(b) and 3(c), respectively. Similarly, the peak-to-peak separation and dip depth are increased until the obstruction radius reaches the critical radius, and then they are decreased.

In the two-peak separation plot [Fig. 3(b)] we note that focus splitting starts at a certain threshold value of the obstruction radius and that this threshold obstruction radius is different for each interface. Interestingly, for the interface between the special coverslip glass and the water, there is a focus-splitting effect present even when there is no obstruction [dashed line in Fig. 3(b)]. However, the corresponding dip depth is less than 0.1%, indicating that the focus-splitting effect is barely detectable in this case. The threshold value of the obstruction radius for the focus-splitting effect is determined by the complicated coupling between the $|E_z|^2$ and the $|E_x|^2$ focal shapes; however, their corresponding dip-depth ratios generally are negligibly small.

Comparing the three different cases of the index-mismatched interface, one can observe that focus splitting is most pronounced in the case of the special coverslip glass ($n = 1.78$)–glass ($n = 1.52$) interface, where the dip-depth ratio η reaches 0.4. In contrast, the interface between the special coverslip glass and the air shows the weakest focus-splitting effect. From these observations, it can be concluded that the focus-splitting effect is stronger for the interface between the two materials with a smaller index difference, provided the obstruction radius is chosen correctly. To see how the change in the NA of an objective affects focus splitting, similar calculations (the peak intensity ratio of $|E_z|^2/|E_x|^2$, the two-peak separation $\Delta\nu$, and the dip-depth ratio η versus the normalized obstruction radius ε) were conducted for two other NA values that are available commercially (NA = 1.2 for a water-immersion objective and NA = 1.4 for an oil-immersion objective) and are presented in Fig. 4. Air is assumed to be the second material throughout the calculations. The corresponding refractive indices of the immersion media are $n = 1.33$ (water) and $n = 1.52$ (oil) for objectives of NA = 1.2 and NA = 1.4. For the case of NA = 1.2, we did not consider the effect of the interface between water and a coverslip because water-immersion objectives are corrected for coverslip aberration. The detailed calculation on focal shape after a beam passes through multiple interfaces can be found elsewhere.[17] It is clear from the Fig. 4 that the strongest focus-splitting

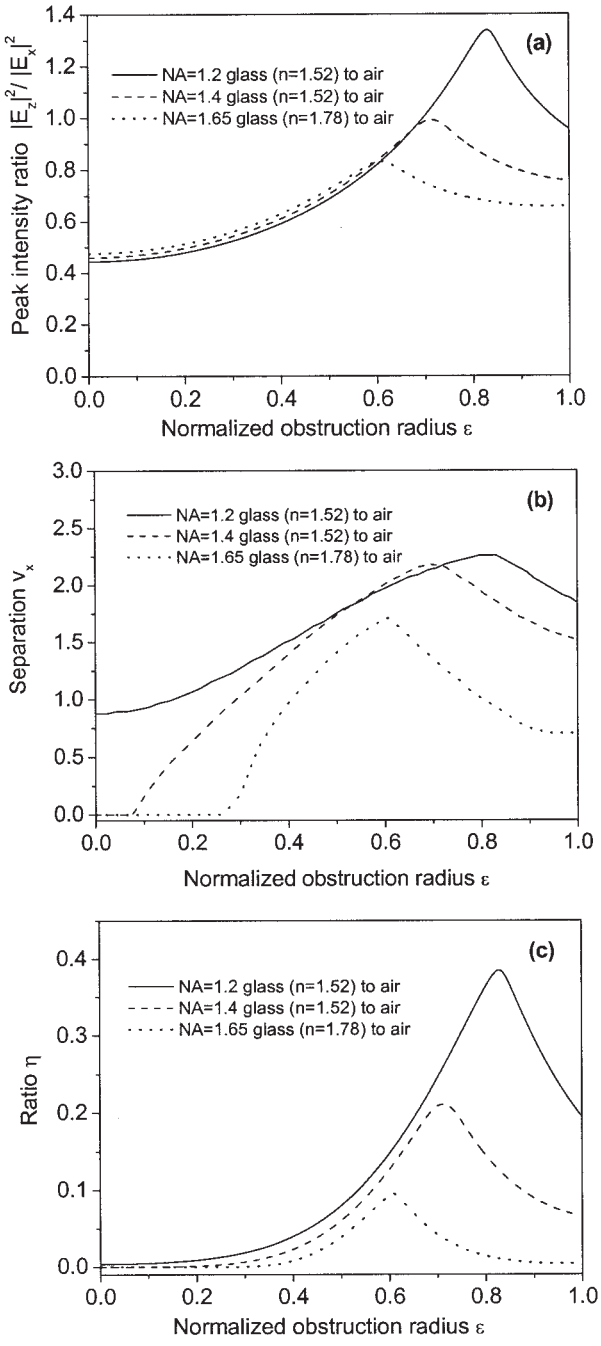

Fig. 4. Plots of (a) the peak intensity ratio of $|E_z|^2/|E_x|^2$, (b) the peak separation $\Delta\nu_x$, and (c) the normalized dip depth η with respect to the normalized obstruction radius ε. The normalized transmitted beam intensity through the index-mismatched interface is shown with respect to the obstruction radius.

effect is observed for the NA-1.2 objective, where the difference between the indices of the two materials (water to air) is the smallest, thus confirming our previous conclusion.

3. Effect of a Detection Pinhole on Image Formation of STIRFM

In Section 2 the detailed theoretical studies predict that the evanescent focus of STIRFM is split into two peaks. However, whether such focus splitting can be directly observed in fluorescence images depends on the detection system and the placement of the pinhole. For one-photon excitation, it is necessary to put a finite-sized pinhole in front of the detection system to reduce the background scattered signal. Consequently, the detection path is confocal in nature, and the effective PSF (denoted by H_{1p})[19] in this case is given by

$$H_{1p} = h_{\mathrm{ill}} h_{\mathrm{det}} \otimes D(v), \tag{6}$$

where h_{ill} is the PSF for illumination and h_{det} is the PSF for detection. The expression for h_{ill} takes the same form as the expression for $|\mathbf{E}|^2$, which is given by

$$h_{\mathrm{ill}} = |\mathbf{E}|^2 = |I_0|^2 + 4|I_1|^2 \cos^2 \phi + |I_2|^2 + 2 \cos 2\phi \mathrm{Re}(I_0 I_2^*) \tag{7}$$

for linearly polarized illumination light ($\lambda = 532$ nm). The expression for h_{det} is given by

$$h_{\mathrm{det}} = |I_0|^2 + 2|I_1|^2 + |I_2|^2 \tag{8}$$

for randomly polarized fluorescence light ($\lambda = 600$ nm). $D(v)$ is the detector (pinhole) function

$$D(v) = \begin{cases} 1 & v < v_d \\ 0 & \text{otherwise} \end{cases}, \tag{9}$$

and $\otimes$ is the two-dimensional convolution operation in a vertical plane. Here v_d is the normalized radius of the detector (pinhole) and is given by

$$v_d = \frac{2\pi}{\lambda_f} r_d \sin \alpha_d, \tag{10}$$

where $\sin \alpha_d$ is the NA of the collector lens in the detection space, λ_f is the fluorescence emission wavelength, and r_d is the radius of the detector.[19] Generally, if the value of v_d is close to zero (a point detector), the detector function $D(v)$ can be taken as the Dirac delta function, and therefore the effective PSF H_{1p} is

$$H_{1p} = h_{\mathrm{ill}} h_{\mathrm{det}}. \tag{11}$$

Similarly, if the detector function is infinitely large, the PSF takes the form

$$H_{1p} = h_{\mathrm{ill}}, \tag{12}$$

owing to the convolution relation.[19]

The contour plot of the PSF H_{1p} for STIRFM with an infinitely large detector (no pinhole) takes the same form as that shown in Fig. 2(d), whereas the STIRFM with a point detector (pinhole) is shown in Fig. 5. One notices that the focus-splitting effect that was previously present in the contour plot of h_{ill} [see Fig. 2(d)] has disappeared. This PSF analysis of STIRFM shows us that the detection of the split focus in a one-photon fluorescence image depends on the size of the pinhole in front of the detector.

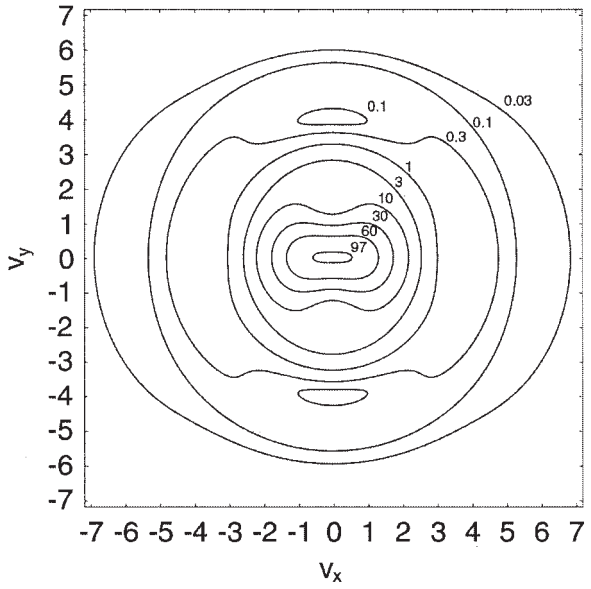

Fig. 5. Contour plot of the effective PSF of the STIRFM [Eq. (10)], with a point detector (pinhole) under one-photon excitation. The incident polarization is from parallel to the x axis. The NA is assumed to be 1.65. The excitation wavelength is 532 nm, and the fluorescence wavelength is 600 nm.

To see the effect of a finite-sized pinhole on the shape of the PSF H_{1p} of STIRFM and to identify the threshold value of v_d for disappearance of the split focus, we calculated the convolution relation in Eq. (6) explicitly. The result is shown in Fig. 6, where the dip-depth ratio η of the split focus is plotted against v_d size. One can see that for $v_d < 4$, the

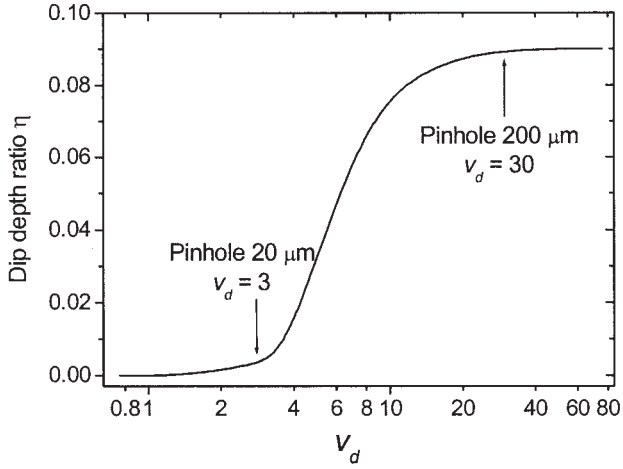

Fig. 6. Plots of the normalized dip depth η with respect to the normalized detector pinhole radius v_d. The actual pinhole sizes used in our experiments are indicated by the two arrows.

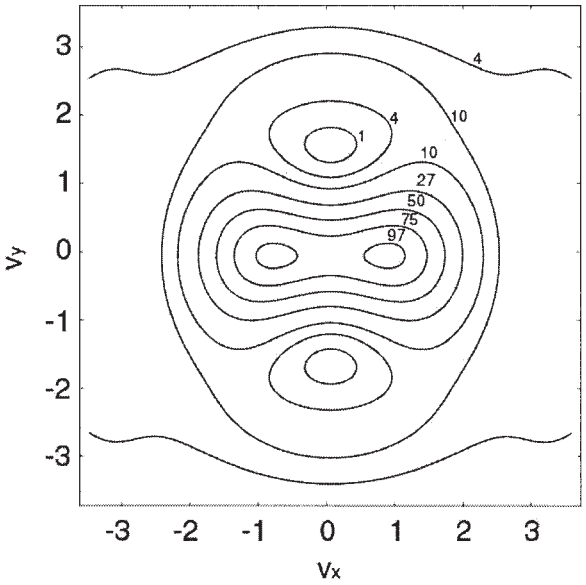

Fig. 7. Contour plot of the effective PSF of the STIRFM under two-photon excitation. The incident polarization is parallel to the x axis. The NA is assumed to be 1.65. The excitation wavelength is 800 nm.

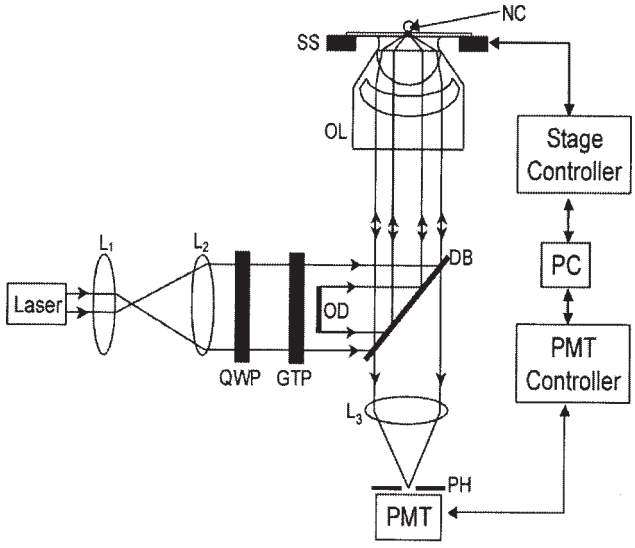

Fig. 8. Experimental setup. Ring-beam illumination is produced by centrally obstructing the circular beam with an opaque disk just before the dichroic beam splitter. QWP, quarter-wave plate; GTP, Glan–Thompson polarizer; OD, obstruction disk; SS, scanning stage; DB, dichroic beam splitter; NC, nanocrystal sample; OL, objective lens (NA = 1.65); PH, pinhole; PC, personal computer.

dip-depth ratio η of the split focus is less than 0.008, making the split focus barely detectable. For $v_d >$ 14, the dip-depth ratio η reaches $\sim$0.1, which is close to the value for the infinitely large detector case [Fig. 2(d)]. Thus $v_d < 4$ can be approximated to be a point detector, whereas $v_d > 14$ can be approximated to be an infinitely large detector. This prediction is validated in Section 4.

For the two-photon excitation case, the pinhole is removed because optical sectioning is intrinsic to two-photon excitation. As a result, the two-photon PSF is

$$H_{2p} = h_{\mathrm{ill}}{}^2. \tag{13}$$

For linearly polarized illumination light (λ = 800 nm), the contour plot of the two-photon PSF H_{2p} is shown in Fig. 7. One observes that the focus-splitting effect is more discernible because the intensity is squared.

In general, image formation in STIRFM is given by the convolution of the fluorescence intensity of a sample with the PSF of the system. As we shall see in Section 4, CdSe quantum dot nanocrystals can be treated as point emitters because their diameter ($\sim$6 nm) is much smaller than the Airy function of the focus (0.5 μm in full width at half-maximum). Therefore the image of quantum dots can be used as the approximate effective PSF for STIRFM and be used to characterize the focal spot.

4. Experimental Characterization of STIRFM

The experimental configuration of STIRFM is shown in Fig. 8. We used a 532-nm diode-pumped cw laser (Spectra-Physics Millenia II) as a one-photon excitation light source, and a Ti:sapphire ultrashort-pulsed laser (Spectra-Physics Tsunami), operating at a wavelength of 800 nm, as a two-photon light source. The laser beam was expanded and focused at the glass–air interface by an objective (NA = 1.65; Olympus). A central obstruction disk (diameter = 4.3 mm, ε_c = 0.62) was inserted just before the reflection at the dichroic beamsplitter, producing a ring-beam illumination. An evanescent field was produced at the focus by obstruction of all the beams with a convergence angle smaller than the critical angle of incidence. Fluorescence produced from the focus was then collected by the same objective and refocused at a photomultiplier tube (Oriel PMT Model 70680) to detect its intensity. For one-photon imaging, a 20 μm diameter (v_d = 3) and a 200 μm diameter (v_d = 30) pinholes were placed in front of the PMT to test the image formation predictions from section III. For two-photon imaging, a 200 μm diameter pinhole (v_d = 30) was used mainly to reduce the background scattered light. For collecting the fluorescence intensity, the sample was scanned in the x and y directions by a scanning stage (Physik Instrumente Model P-517.3CL) to build up a two-dimensional fluorescence image. A special coverslip glass and immersion oil for the NA-1.65 objective had a refractive index of 1.78. The high refractive index of the immersion oil and the coverslip glass increases the portion of the objective exit pupil in producing an evanescent field. For comparison, Table 1 shows the total internal reflection angles and the maximum convergence angles of three different high-NA objectives, as well as the ratio of the critical obstruction radius to the exit pupil radius (ε_c) for the total internal reflection. It is clear from the table that the

Table 1. Comparison of the Cutoff Angle for Total Internal Reflection in Various Objectives[a]

Objective Type	NA	Refractive Index of Immersion Medium	Maximum Angle of Convergence (deg)	Cutoff Angle for TIR in Water (deg)	ε_c in Water	Cutoff Angle for TIR in Air (deg)	ε_c in Air
Water immersion	1.2	1.52	64	61	0.97	41	0.73
Oil immersion	1.4	1.52	67	61	0.92	41	0.71
Special oil immersion	1.65	1.78	68	48	0.80	34	0.60

[a] ε_c refers to the critical obstruction radius ratio (ε = obstruction radius/exit pupil radius).

critical angle for the total internal reflection for NA = 1.65 is significantly lower than that of the other objectives, increasing the portion of the objective exit pupil for producing an evanescent field. This large portion provides more freedom in manipulating the evanescent field properties such as field depth and strength. It should be noted that a similar geometry was proposed for scattering surface plasmon polaritons for a thin metal film coated at the interface to excite the surface plasmons.[20] However, the heating of the metal film associated with this geometry poses a significant problem for biological applications.

To characterize the focal spot shape and evanescent field depth control of the STIRFM, two different fluorescent samples were utilized. For the focal spot characterization, CdSe quantum dot nanocrystals capped with trioctylphosphine oxide and trioctylphosphine were used. The quantum dots are ideal for characterizing the focal spot because of their small size and their negligible excitation polarization selection, which makes them the isotropic absorber of the field. The method of the nanocrystal preparation has been published elsewhere.[21] The mean diameter of the nanocrystals was ~6 nm, and the peak fluorescence wavelength was at 600 nm. The nanocrystals were diluted in chloroform, and a small droplet of the solution was dried onto a cleaned special coverslip glass. The average density of the quantum dots on the coverslip was calculated from the solution concentration, the droplet volume, and the dried area on the coverslip and was found to be 1 quantum dot/μm^2. For the measurements of the evanescent field depth with respect to the obstruction disk radius, Rhodamine 6G–doped microbeads of 6-μm diameter were used. Because the evanescent field only propagates ~200 nm into the second medium, the microbeads could not be imaged at their equatorial plane, and only the caps of the beads that were immersed in an evanescent field were imaged. As we increased the obstruction disk diameter, the diameter of the bead caps in the image was decreased, indicating a decrease in the evanescent field depth. A schematic depiction of beads being excited only at their caps is shown in Fig. 9. Using simple geometry, the following approximate relation between the

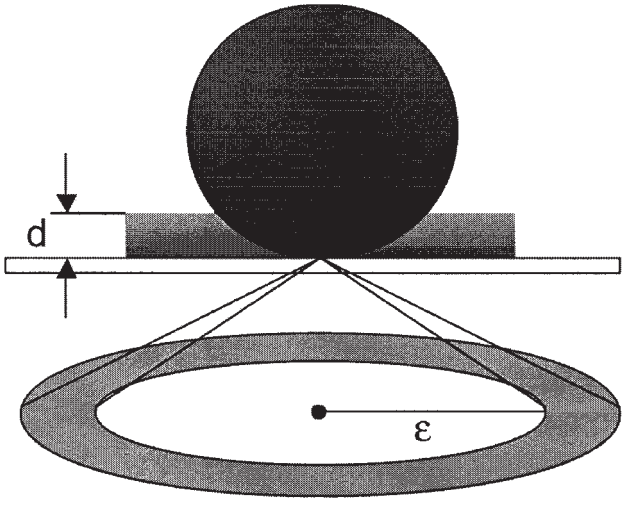

Fig. 9. Cross-section view of the microbeads excited with an evanescent field. ε is the obstruction radius.

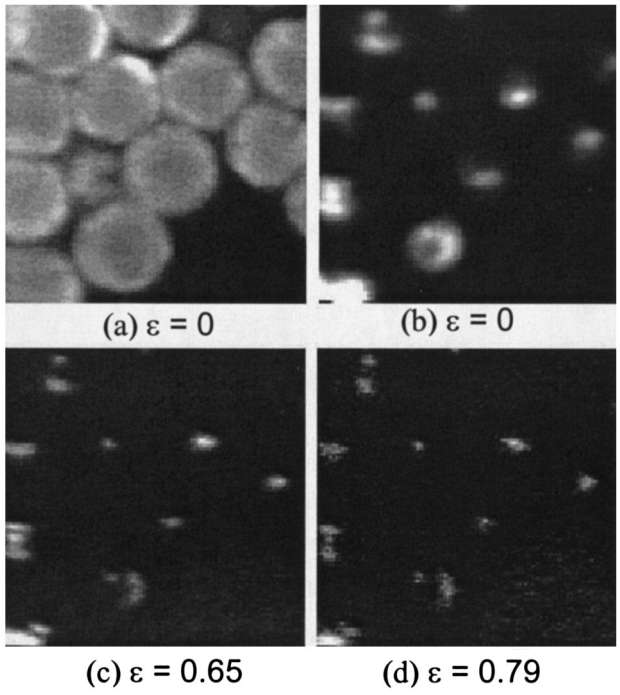

Fig. 10. Images of Rhodamine 6G microbead images (20 μm × 20 μm, excitation at 532 nm): (a) confocal image around the equatorial plane of the beads, (b) confocal image at the interface between coverslip glass and air, (c) STIRFM image with ε = 0.65 (ε_c = 0.6), (d) STIRFM image with ε = 0.79.

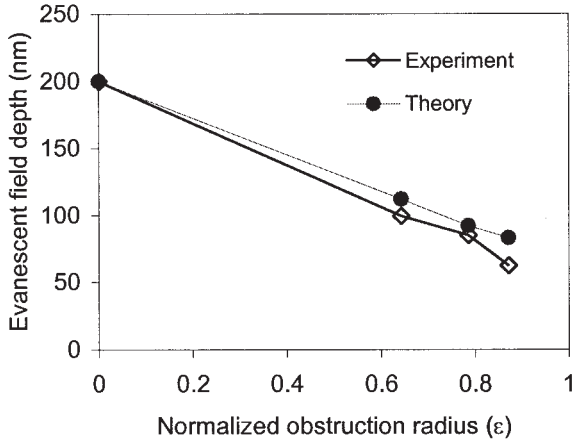

Fig. 11. Evanescent field depth as a function of the central obstruction size.

diameter a of the cap image and the evanescent field depth d may be derived

$$d = r - [r^2 - (a/2)^2]^{1/2}, \tag{14}$$

where r is the radius of the bead. Here the diameter a of the cap image is defined by the full width at half-maximum of the bead image. With Eq. (14) the relative evanescent field depths were measured with respect to the obstruction disk size.

Figure 10 shows the one-photon fluorescence images of Rhodamine 6G microbeads in confocal microscopy and STIRFM. Figs. 10(a) and 10(b) are confocal images of the microbeads around the equatorial plane and at the interface, respectively. The image at the interface [see Fig. 10(b)] shows that many of the beads are still clearly visible because of the propagating light ($\theta > \theta_c$). In comparison, the STIRFM images with two values of obstruction [Figs. 10(c) and 10(d)] clearly show that only the bead caps are visible, demonstrating the capability of the background fluorescence suppression of STIRFM. From the images we can calculate the evanescent field depths according to Eq. (14) and as a function of the obstruction radius (Fig. 11). As predicted, the evanescent field depth decreases with increasing obstruction radius. The theoretical simulation results of the evanescent field depth with Eq. (1) are also plotted in the same figure. A comparison between the theoretical predictions and the experimental results show good agreement, indicating that the evanescent field depth can be controlled with STIRFM.

The images of CdSe quantum dots in one-photon and two-photon STIRFM modes are shown in Fig. 12. Because of the small size of the evanescent focus, there may be more than one quantum dot present and, for that reason, the emission dark axis of a single quantum dot[22] was not considered in the image formation. For one-photon excitation, images are taken with two pinhole sizes (20 and 200 μm). One notices that the focus-splitting effect is absent for the image with a small pinhole detector [see Fig. 12(a)], whereas it is clearly present for a large-pinhole detector [see Fig. 12(b)]. The theoretical PSFs for each case are also shown. The small-pinhole image was approximated with the point detector function, whereas the large-pinhole image was approximated with the infinitely large detector function. Each case shows good agreement with the experimental focal shapes. Optical resolution of the system was taken from the full width at half-maximum of the focal profile in the direction perpendicular to the polarization direction. The measured value in the small-pinhole case is ~150 nm, whereas the theoretical value is 140 nm. This demonstrates a good transverse resolution of the system. The two-photon image of CdSe quantum dots is also shown in Fig. 12. It is clear that the focus splitting is larger and more distinctive here than in the one-photon case, and it shows good agreement with the theoretical simulation. This demonstrates that the highly focused evanescent field of STIRFM and its image formation under one-photon and two-photon excitation can be accurately predicted.

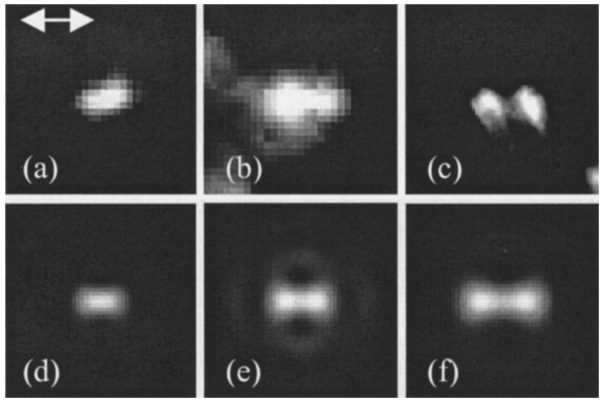

Fig. 12. (a)–(c) Experimental images (1 μm × 1 μm) of CdSe quantum dot nanocrystals in STIRFM. (d)–(f) Theoretical simulations of the focal spot image in STIRFM. (a) One-photon fluorescence image with 20-μm pinhole detection. (b) One-photon image with 200-μm pinhole detection, with excitation at 532 nm and power of 0.2 kW/cm^2. (c) Two-photon fluorescence image with 200-μm pinhole detection, with excitation at 800 nm and power of 0.2 MW/cm^2. (d) Theoretical one-photon fluorescence image with a point detector. (e) Theoretical one-photon fluorescence image with an infinitely large area detector. (f) Theoretical two-photon fluorescence image with an infinitely large area detector. Conditions are assumed to be identical to the experimental cases. The arrow indicates the direction of the incident polarization.

5. Conclusions

In this paper a new type of total internal reflection fluorescence microscopy called STIRFM, which utilizes ring-beam illumination and a high-NA objective, has been proposed. The focused evanescent field in STIRFM can confine the excitation in a small volume, thus effectively shunning the background noise from both lateral and axial directions. The experimental images of CdSe quantum dot nanocrystals and dye-doped microbeads have been presented and show that the lateral resolution and the depth of the fo-

cused evanescent field of STIRFM can be well characterized and controlled. A rigorous theoretical investigation of the electric field structure near the focus in STIRFM has shown focus splitting due to depolarization. An appropriate PSF analysis of the system has been provided for the interpretation of the quantum dot images and the focus-splitting effect. To increase the transverse resolution and to remove the elongation of the focal spot in STIRFM, one can use the apodization method for a lens of the future.[23]

It is expected that STIRFM will play an important role in the area of single molecular detection; near-interface fluorescence kinetic studies; fluorescence lifetime imaging; and near-field applications, such as near-field trapping, near-field fabrication, and two-photon near-field microscopy.

The authors thank Paul Mulvaney and Craig Bullen of the School of Chemistry, The University of Melbourne, for CdSe quantum dot samples and for many interesting discussions. The authors also acknowledge support from the Australian Research Council.

References

1. H. Watarai and F. Funaki, "Total internal reflection fluorescence measurements of protonation equilibria of Rhodamine B and Octadecylrhodamine B at a toluene/water interface," Langmuir **12,** 6717–6720 (1996).
2. M. Toriumi and M. Yanagimachi, "Time-resolved total-internal-reflection fluorescence spectroscopy and its applications to solid/polymer interface layers," in *Microchemistry, Spectroscopy and Chemistry in Small Domains*, H. Masuhara, F. De Schryver, N. Kitamura, and N. Tamai, eds. (Elsevier, New York, 1994), pp. 257–268.
3. K. Stock, R. Sailer, W. S. L. Strauss, R. Pavesi, M. Lyttek, H. Emmert, and H. Schneckenburger, "Total internal reflection fluorescence spectroscopy and microscopy (TIRFS/TIRFM) in cell biology and photobiology," in *Fluorescence Microscopy and Fluorescent Probes*, A. Kotyk, ed. (Espero Publishing, Prague, 1999), Vol. 3, pp. 67–79.
4. R. Sailer, K. Stock, W. S. L. Strauss, M. Lyttek, and H. Schneckenburger, "Total internal reflection fluorescence microscopy (TIRFM) of acridine orange in single cells," Endocytobiosis & Cell Res. **14,** 129–136 (2001).
5. W. P. Ambrose, P. M. Goodwin, and J. P. Nolan, "Single-molecule detection with total internal reflection excitation: comparing signal-to-background and total signals in different geometries," Cytometry **36,** 224–231 (1999).
6. M. F. Paige, E. J. Bjerneld, and W. E. Moerner, "A comparison of through-the-objective total internal reflection microscopy and epi-fluorescence microscopy for single-molecule fluorescence imaging," Single Mol. **2,** 191–201 (2001).
7. M. Tokunaga, K. Kitamura, K. Saito, A. H. Iwane, and T. Yanagida, "Single molecule imaging of fluorophores and enzymatic reactions achieved by objective-type total internal reflection fluorescence microscopy," Biochem. Biophys. Res. Commun. **235,** 47–53 (1997).
8. T. Funatsu, Y. Harada, M. Tokunaga, K. Saito, and T. Yanagida, "Imaging of single fluorescent molecules and individual ATP turnovers by single myosin molecules in aqueous solution," Nature **374,** 555–559 (1995).
9. R. D. Vale, T. Funatsu, D. W. Pierce, L. Romberg, Y. Harada, and T. Yanagida, "Direct observation of single kinesin molecules moving along microtubules," Nature **380,** 451–453 (1996).
10. T. Wazawa, Y. Ishii, T. Funatsu, and T. Yanagida, "Spectral fluctuation of a single fluophore conjugated to a protein molecule," Biophys. J. **78,** 1561–1569 (2000).
11. Y. Sako, S. Minoghchi, and T. Yanagida, "Single-molecule imaging of EGFR signaling on the surface of living cells," Nat. Cell Biol. **2,** 168–172 (2000).
12. R. M. Dickson, D. J. Norris, Y. L. Tzeng, and W. E. Moerner, "Three-dimensional imaging of single molecules solvated in pores of poly(acrylamide) gels," Science **274,** 966–968 (1996).
13. B. Sick, B. Hecht, and L. Novotny, "Orientational imaging of single molecules by annular illumination," Phys. Rev. Lett. **85,** 4482–4485 (2000).
14. B. Sick, B. Hecht, U. P. Wild, and L. Novotny, "Probing confined fields with single molecules and vice versa," J. Microsc. **202,** 365–373 (2000).
15. L. Novotny, M. R. Beversluis, K. S. Youngworth, and T. G. Brown, "Longitudinal field modes probed by single molecules," Phys. Rev. Lett. **86,** 5251–5254 (2001).
16. P. Török, P. Varga, Z. Laczik, and G. R. Booker, "Electromagnetic diffraction of light focused through a planar interface between materials of mismatched refractive indices: an integral representation," J. Opt. Soc. Am. A **12,** 325–332 (1995).
17. M. Gu, *Advanced Optical Imaging Theory* (Springer, Heidelberg, 2003).
18. J. W. M. Chon, X. Gan, and M. Gu, "Splitting of the focal spot of a high numerical-aperture objective in free space," Appl. Phys. Lett. **81,** 1576–1578 (2002).
19. M. Gu, *Principles of Three-Dimensional Imaging in Confocal Microscopy* (World Scientific, Singapore, 1996).
20. H. Kano, S. Mizuguchi, and S. Kawata, "Excitation of surface-plasmon polaritons by a focused laser beam," J. Opt. Soc. Am. B **15,** 1381–1386 (1998).
21. C. B. Murray, D. J. Norris, and M. G. Bawendi, "Synthesis and characterization of nearly monodisperse CdE (E = S, Se, Te) semiconductor nanocrystallites," J. Am. Chem. Soc. **115,** 8706–8715 (1993).
22. S. A. Empedocles, R. Neuhauser, and M. G. Bawendi, "Three-dimensional orientation measurements of symmetric single chromophores using polarization microscopy," Nature **399,** 126–130 (1999).
23. G. Toraldo di Francia, "Super-gain antennas and optical resolving power," Nuovo Cimento Suppl. **9,** 426–428 (1952).